Talanta 275 (2024) 126104

Contents lists available at ScienceDirect

Talanta

journal homepage: www.elsevier.com/locate/talanta

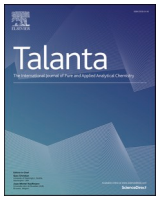

Vibrational spectroscopy coupled with machine learning sheds light on the cellular effects induced by rationally designed TLR4 agonists

Diletta Ami [a,1], Ana Rita Franco [a,1], Valentina Artusa [a], Alessio Romerio [a], Mohammed Monsoor Shaik [a], Alice Italia [a], Juan Anguita [b,c], Samuel Pasco [b], Paolo Mereghetti [d], Francesco Peri [a,**], Antonino Natalello [a,*]

[a] Department of Biotechnology and Biosciences, University of Milano-Bicocca, Piazza della Scienza, 2, 20126, Milano, Italy
[b] Center for Cooperative Research in Biosciences (CIC bioGUNE), Basque Research and Technology Alliance (BRTA), 48160, Derio, Bizkaia, Spain
[c] Ikerbasque, Basque Foundation for Science, Plaza Euskadi 5, 48009, Bilbao, Bizkaia, Spain
[d] Bioinformatics Consultant, 15061, Arquata Scrivia, Italy

ARTICLE INFO

Handling Editor: Prof. J. Wang

Keywords:
FTIR microspectroscopy
Lipopolysaccharide
Multivariate analysis
Spectroscopic fingerprint
TLR4 agonists

ABSTRACT

In this work, we present the potential of Fourier transform infrared (FTIR) microspectroscopy to compare on whole cells, in an unbiased and untargeted way, the capacity of bacterial lipopolysaccharide (LPS) and two rationally designed molecules (FP20 and FP20Rha) to activate molecular circuits of innate immunity. These compounds are important drug hits in the development of vaccine adjuvants and tumor immunotherapeutics. The biological assays indicated that FP20Rha was more potent than FP20 in inducing cytokine production in cells and in stimulating IgG antibody production post-vaccination in mice. Accordingly, the overall significant IR spectral changes induced by the treatment with LPS and FP20Rha were similar, lipids and glycans signals being the most diagnostic, while the effect of the less potent molecule FP20 on cells resulted to be closer to control untreated cells. We propose here the use of FTIR spectroscopy supported by artificial intelligence (AI) to achieve a more holistic understanding of the cell response to new drug candidates while screening them in cells.

1. Introduction

Modulating the molecular circuits of innate and adaptive immunity is a key target of innovative immunotherapeutics and vaccines [1]. Developing molecules capable of this modulation, with defined mechanisms of action, is of high relevance to develop effective immune-based therapies. An important class of molecules in preclinical and clinical development phase as vaccine adjuvants and tumor immunotherapeutics are compounds that stimulate the human innate immunity receptor TLR4 (Toll-Like Receptor 4) thus mimicking the action of lipid A, the natural TLR4 agonist [2,3]. Lipid A, the lipid portion of bacterial lipopolysaccharide (LPS), binds to the receptor dimer TLR4/MD-2 on the cell surface with the intervention of CD14 coreceptor thus initiating MyD88 and TRIF signalling, leading respectively to the production of inflammatory cytokines and type I interferon [4]. These intracellular activations cause a switch in macrophage phenotype and metabolism. Macrophages that have been activated by LPS possess an M1 phenotype, are called classically activated and secrete several proinflammatory cytokines and chemokines [5].

We have recently applied Fourier transform infrared (FTIR) microspectroscopy - obtained by the coupling of an infrared microscope to a FTIR spectrometer - to the study of the LPS-induced inflammation in intact human macrophage-like cells [6]. Although FTIR analyses of other inflammation models have been published [7,8], our study is the first in which FTIR has been applied to investigate the complex molecular effects caused by LPS stimulation in human macrophages derived from THP-1 monocytes.

FTIR spectroscopy is a powerful tool to monitor, in a non-destructive

Abbreviations: AI, Artificial Intelligence; FTIR, Fourier Transform Infrared; GAGs, Glycosaminoglycans; hTLR, human Toll Like Receptor; LPS, Lipopolysaccharide; MPLA, Monophosphoryl Lipid A; Nnet, Neural Network; OVA, Ovalbumin; PLS-DA, Partial Least Squares-Discriminant Analysis; SEAP, Secreted Embryonic Alkaline Phosphatase; TDMs, THP-1 derived macrophages; TLR, Toll Like Receptor.

* Corresponding author.
** Corresponding author.
E-mail addresses: francesco.peri@unimib.it (F. Peri), antonino.natalello@unimib.it (A. Natalello).
[1] These Authors contributed equally.

https://doi.org/10.1016/j.talanta.2024.126104
Received 24 January 2024; Received in revised form 4 April 2024; Accepted 11 April 2024
Available online 17 April 2024

and label-free way, the global biochemical composition of whole cells through the absorption of electromagnetic radiation in the mid-infrared range. This vibrational spectroscopy technique probes a large number of molecules simultaneously and its sensitivity to structural and compositional changes makes it complementary to other biochemical methods. For these reasons, FTIR spectroscopy has become an attractive tool in molecular and cellular biophysics with important applications also in biomedical research [9–12]. Given the complexity of IR spectra resulting from the overlapping absorptions of the main cell biomolecules (i.e. lipids, proteins, nucleic acids and carbohydrates), their interpretation requires a sophisticated multivariate analysis able to point out significant and non-redundant information [13–15].

The main findings of our previous work [6] are represented by the identification of different classes of intracellular molecules that stand out as the most affected by LPS stimulation. Our previously published study can be considered a first step in the direction to associate a well-defined and reproducible spectroscopic IR pattern to a complex biological effect produced by a bioactive molecule in cells [6].

The goal in our current research was to investigate the potential of FTIR spectroscopy, supported by machine learning approaches, to compare the biological effects of natural and two synthetic TLR4 agonists. This was achieved by comparatively assessing the degree to which each of the agonists affected the molecular pathways in whole cells.

In particular, our group developed synthetic TLR4 agonists deriving from the molecular simplification of monophosphoryl lipid A (MPLA), a chemically modified, non-toxic lipid A variant (Fig. 1). These molecules, called FP compounds, have a glucosamine monosaccharide core instead of the disaccharide of MPLA, with a simplified synthesis [16]. FP compounds, similarly to MPLA, activate TLR4 , *in vitro* and *in vivo* [2,16,17] (Fig. 1). The recently developed FP20 and FP20Rha are active in stimulating TLR4. FP20Rha (Fig. 1) contains a rhamnose monosaccharide unit linked to FP20 C-6 that mimics the first Kdo unit of the LPS core oligosaccharide [18]. The presence of the additional monosaccharide unit gives an increase of activity in FP20Rha, compared to FP20, in stimulating the TLR4-dependent cytokine production. Here, we investigated by cell biology techniques and FTIR microspectroscopy the response of whole THP-1 derived human macrophages (TDMs) after treatment with FP20Rha and we compared the molecular effects induced in cells by this compound with that of FP20 and LPS as a reference compound. The FTIR spectroscopy supported by the multivariate analysis, validated by *in vitro* and *in vivo* characterizations, allowed to assess, in a non-biased way, the similarity of the effect of FP20Rha and natural LPS in triggering inflammation and early innate immune response in cells.

In principle, this comparative FTIR assessment allows the identification of drug hit candidates while simultaneously gathering mechanistic insights in an easier, faster, and less expensive way. The proof of concept presented here could be extended to the screening of bioactive hit compounds with the aim to assess their capacity to affect in a reproducible way complex phenomena associated with multiple molecular pathways.

2. Methods

2.1. TLR4 vs TLR2 selectivity and TLR4 activity in macrophages

The selective activity of LPS, FP20, and FP20Rha towards the human TLR4 (hTLR4) receptor was assessed using HEK Blue hTLR4 and hTLR2 reporter cell lines, as previously reported [16,17,19]. Briefly, these cells have been transfected with genes encoding either for the hTLR4 or hTLR2 receptors as well as a reporter gene encoding for secreted embryonic alkaline phosphatase (SEAP). Cells were treated with increasing concentrations of FP20 and FP20Rha. Smooth (S)-form LPS (S-LPS) and MPLA from *Salmonella minnesota* were used as positive controls for hTLR4 activation, while Pam2CysSerLys4 (PAM2CSK4) was used as a positive control for hTLR2 activation. HEK Blue hTLR2 cells were also exposed to S-LPS, as it is reported by the manufacturer that LPS results in mild activation of these cells. Results were normalized to the positive control by attributing 100 % activation to it. TLR4 activity in macrophages was studied using THP-1 X Blue derived macrophages (TDMs) [16,17,19]. Activation of these macrophage-like cells was assessed by measuring SEAP secretion. THP-1 X-Blue cells were transfected with an NF-κB/AP-1-inducible SEAP gene construct. When TLR4 is activated, the downstream signalling cascade is initiated leading to NF-κB and AP-1 transcription and consequent SEAP release. Results were normalized to the positive control by attributing 100 % activation to it. TDM cytokine profile was determined using Enzyme-Linked Immunosorbent Assay (ELISA). Briefly, TDM were treated for 3, 6 and 18 h with 10 μM of FP20 or FP20Rha and with positive control 100 ng/mL of S-LPS. Supernatant was collected at the mentioned time points and TNF, IL-6 and IL-1β levels were measured. Experimental details on cell cultures, on treatments for cell reporter assays, and cytokine detection are reported

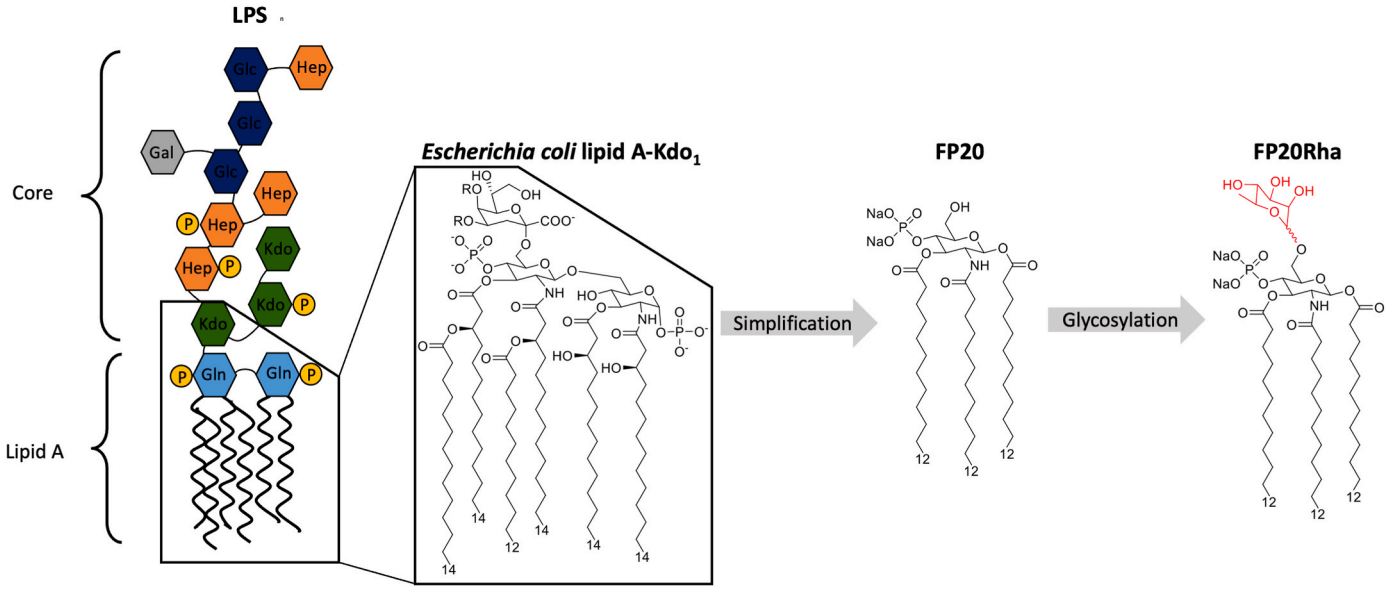

Fig. 1. Structure of LPS and FP derivatives. Molecular simplification of gram-negative bacterial LPS into synthetic molecules FP20 and FP20Rha. Compared to FP20, FP20Rha mimics a more extended part of LPS, including the Kdo unit of the core oligosaccharide.

in the Supplementary Methods.

2.2. In vivo adjuvant activity

In vivo adjuvant activity was studied as previously reported [16,17,19]. Briefly, C57BL/6 mice were injected subcutaneously on day 0 with 10 μg of Ovalbumin (OVA) formulated with 10 μg of commercially available MPLA or FP20Rha or no adjuvant. A boost immunization was performed on day 22. Total anti-OVA IgG levels were assessed on day 21 and on day 42 using Enzyme-Linked Immunosorbent Assay (ELISA). See Supplementary Methods for details.

2.3. FTIR microspectroscopy analysis of intact TDM cells

Cell samples for FTIR analysis have been prepared following a procedure previously optimised [6,20]. Briefly, after differentiation of THP-1 X-Blue to TDMs by exposure to 100 ng/mL of PMA for 72 h [6], cells were treated with 10 μM of FP20 or FP20Rha for 15 min, 3 h and 24 h. Untreated and LPS-treated cells have been also analysed as negative and positive controls, respectively [6]. After exposure to the compounds, cells were washed with PBS (Euroclone), scraped using a cell scraper and collected into centrifuge tubes. After centrifugation at 4 °C for 10 min at approximately 125×*g*, PBS was discarded and cell pellets were resuspended in physiological solution (NaCl 0.9 %) for further centrifugation at 4 °C, 5 min at 125×*g*. This washing step was repeated 3 times to ensure no medium contamination. Afterwards live cells were resuspended in ~10 μL of physiological solution immediately prior to FTIR measurements. About 3 μL of cell suspension were deposited onto a IR-transparent BaF_2 window and dried at room temperature, in a laminar flow hood, for at least 30 min to eliminate the excess of water. FTIR absorption spectra were acquired in transmission mode, between 4000 and 700 cm^{-1}, by a Varian 610-IR infrared microscope coupled to the Varian 670-IR FTIR spectrometer (both from Varian Australia Pty Ltd., Mulgrave VIC, Australia), equipped with a mercury cadmium telluride, nitrogen-cooled detector. The variable microscope aperture was adjusted to 100 μm × 100 μm (spatial resolution). Measurements were performed at 2.0 cm^{-1} spectral resolution, 25 KHz scan speed, triangular apodization, and by the accumulation of 512 scan co-additions. For comparison, after water vapor correction [20] when necessary, absorption spectra were normalized at the Amide I band area (Figure S1) and the second derivative analysis was performed, after a 13-point smoothing of the measured spectra, by the Savitzky–Golay method (3rd polynomial, 9 smoothing points), using the GRAMS/32 software (Galactic Ind. Corp., Salem, NH, USA). To investigate spectral heterogeneity different areas on the same sample have been measured and to evaluate the reproducibility of the results at least three independent experiments have been performed.

2.4. Multivariate data analysis

Multivariate analysis has been performed using R version 3.6.3 [21].

2.4.1. Neural networks classification

The second derivatives of the FTIR absorption spectra have been split into four spectral ranges (3050-2800, 1800-1500, 1500-1200, 1200-800 cm^{-1}) and neural networks (nnet) have been applied on each region. In particular, the nnet method implemented in the Caret package version 6.0–93 has been used [22]. In order to assess the predictive discrimination and avoid over-fitting, for each method a 3-time repeated 5-fold cross-validation was applied. In this way, for each method 15 models were trained. Since for each sample multiple spectra have been collected, folds have been created at the sample level, ensuring that all spectra for a given sample are either in the training or in the test set. More specifically, having N samples each with m_N spectra, on every round of cross-validation, the samples have been partitioned into 5 folds. Four folds (containing N*4/5 samples) have been used to train the model and the remaining fold (containing N*1/5 samples) was used to test the model. Folds are complementary (i.e. no repeated samples in different folds) and the samples are randomly chosen. The training of the model is repeated five times, each time varying the test partition. The 5-fold cross-validation is then repeated 3-times in order to lower the risk of partition-dependent artefacts. The best model has been selected using the "one standard error rule". In this case, the model with the best performance value is identified and, using resampling, we can estimate the standard error of performance. The final model used was the simplest model within one standard error of the (empirically) best model [23].

As a performance measure, the accuracy, e.g. the proportion of true results (true positive + true negative) over the total number of samples, was used. All spectra have been center-scaled (normalized in order to have 0 mean and variance 1) to allow faster convergence of the training algorithm and improve the numerical stability.

The number of hidden layers in the neural network was kept fixed to 2, while the decay parameter was varied (0.4, 0.6, 0.8) during training. Network with the highest accuracy was selected. The maximum number of iterations was set to the value of 5000. For the best model, the normalized (0–1) confusion matrix was computed.

Variable importance has been computed using the Garson/Goh algorithm [24,25].

2.4.2. PLS-DA on selected wavenumbers

Partial least squares discriminant analysis (PLS-DA) is a widely used multidimensional linear regression method, which is a variant of the classical partial least square method when the dependent variable is categorical [26]. The PLS-DA model includes the following 13 classes: not treated (NT), LPS, FP20Rha, FP20 each at 15 min, 3h, 24h, plus the NT at time 0. A set of intensities at selected wavenumbers has been used as independent variables.

The discrimination accuracy among the classes was evaluated using the classification accuracy, e.g. the proportion of true results (true positive + true negative) over the total number of samples. The distribution of distances between treated and untreated cells has been obtained by computing the Euclidean distance between all pairs of spectra (in the low dimensional PLS score space), using the NT at time 0 as reference, that is:

$$D_{K,i,j} = \frac{1}{L}\sqrt{\sum_{c=1}^{L}\left(x_{K,j,c}\text{-}r_{i,c}\right)^2}$$

where r_i is the i-th spectra belonging to the reference group (NT at 0h), while x_j(K) is the j-th spectra belonging to the treated groups (and the NT) at each time point, e.g K = [NT 15 min, NT 3h, NT 24h, FP2Rha 15 min, LPS 15 min, LPS 3h, LPS 24h, FP2Rha 15 min, FP2Rha 3h, FP2Rha 24h, FP20 15 min, FP20 3h, FP20 24h]. L is the number of PLS scores and c is the c-th PLS component.

2.4.3. Multivariate analysis of variance (MANOVA)

MANOVA was applied to selected wavenumbers. MANOVA tests whether mean differences among groups on a combination of dependent variables are likely to have occurred by chance [27]. In this case, a two-ways mixed-model MANOVA (within-between subjects MANOVA) was applied, where treatment (NT, LPS, FP20Rha, FP20) is the between-subjects independent variable, time (0h, 15 min, 3h, 24h) is the within-subject independent variable and the intensities at the selected wavenumbers are the dependent variables. The Pillai's Trace was used as a statistical test because it is robust and better for unbalanced design. The analysis is carried on considering also the interactions between treatment and time (full MANOVA results are reported in Table S1). Preliminary tests for the MANOVA validity have been performed: absence of multicollinearity (the dependent variables cannot be too correlated, correlation must be lower than 0.90 [27], multivariate normality, homogeneity of variance-covariance matrices).

2.4.4. Post-hoc analysis

Pairwise comparisons have been performed using t-tests with pooled standard deviation and p-values were computed using Holm's correction [27]. For each selected variable, pairwise t-tests were computed between the NT at a given time (15 min, 3h, 24h) and the treated group (LPS, FP20Rha, FP20) at the same time. See Table S1 for detailed results.

3. Results and discussion

3.1. TLR4 vs TLR2 selectivity and TLR4 activity in macrophages

The selective activity of FP20Rha towards the hTLR4 receptor was assessed using HEK Blue hTLR4 (Fig. 2**a**) and hTLR2 (Fig. 2b) reporter cell lines. As expected, FP20Rha, as well as FP20, activated the hTLR4 receptor and not hTLR2 (Fig. 2**a-b**). Following this initial screening, THP-1 X-Blue derived macrophages (TDMs) were used to compare immunostimulating properties of FP20, FP20Rha and S-LPS. As shown in Fig. 2c, FP20Rha activates TDMs in a dose-dependent manner and at the 10 μM concentration shows the same level of activity as S-LPS. Fig. 2d–f shows the proinflammatory cytokine profile of S-LPS, FP20 and FP20Rha at 3, 6 and 18h measured using Enzyme-Linked Immunosorbent Assay (ELISA). Very similar trends are observed between S-LPS and FP20Rha in the induction of TNF and IL-1β production along the different time points (Figs. 2d and 2f). While lower than S-LPS, also IL-6 production induced by FP20Rha follows the same pattern of increase over time (Fig. 2e).

3.2. In vivo adjuvant activity

To further understand the immunostimulatory properties of FP20Rha, we performed a vaccine study in C57BL/6 mice, using ovalbumin (OVA) as antigen without adjuvant or with FP20Rha or MPLA as adjuvant. A boost immunization was performed on day 22. Total anti-OVA IgG levels were assessed on day 21 (Fig. 3a) and on day 42 (Fig. 3b). Pre-boost results show that FP20Rha is able to induce half of the anti-OVA antibodies in respect to MPLA. However, looking at final total anti-OVA IgG values, it is possible to observe that FP20Rha performs slightly better than MPLA. As previously reported [17], FP20, in the same experimental conditions, was able to induce specific anti-OVA IgG at 1 AUC while FP20Rha induced at a magnitude of 6 AUC. These results further confirm that FP20Rha is active as a vaccine adjuvant with a potency similar to MPLA.

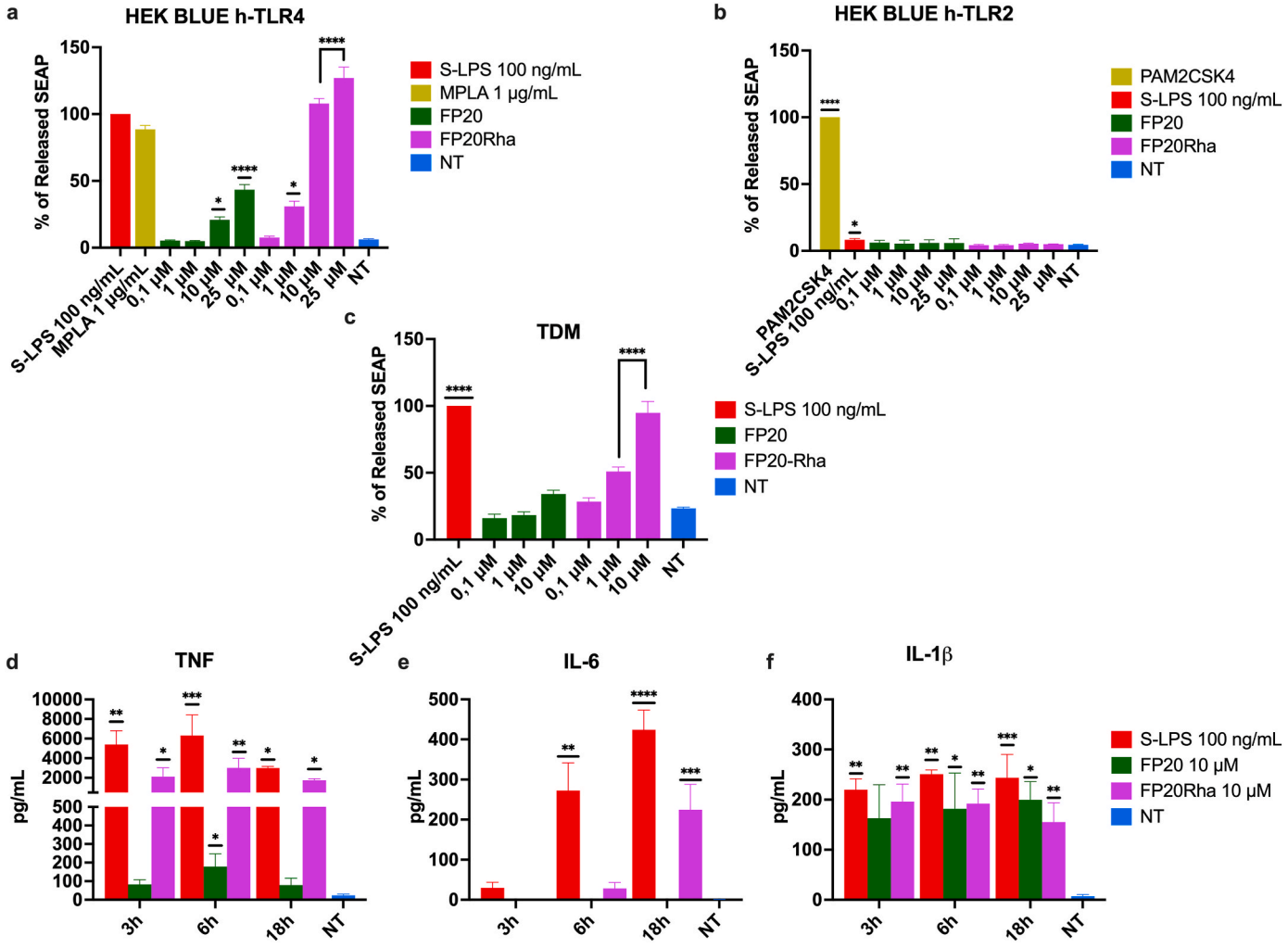

Fig. 2. ***In vitro*** **activity of LPS and FP derivatives. a-c**) Selectivity towards hTLR4 in HEK cells and activity in TDMs. HEK-Blue hTLR4 cells (a) and HEK-Blue TLR2 (b) were treated with the shown concentrations of FP20, FP20Rha, MPLA (1 μg/mL), S-LPS (100 ng/mL), and Pam2CSK4 (10 ng/mL), and incubated for 16–18 h. (c) TDM cells were treated with the shown concentrations of FP20, FP20Rha and incubated for 16–18 h. S-LPS (100 ng/mL) was used as control. 100 % stimulation has been assigned to the positive control S-LPS (a and c) or Pam2CSK4 (b). **d-f**) Cytokine profile on TDMs at 3, 6 and 18 h. TDMs were treated with 10 μM of FP20 and FP20Rha or with 100 ng/mL of S-LPS for the shown time points. Supernatant was collected and TNF, IL-6 and IL-1β levels were measured by ELISA. Data are expressed as mean ± SEM of at least three independent experiments (treated vs not treated: *P < 0.05; **P < 0.01; ***P < 0.001; ****P < 0.0001).

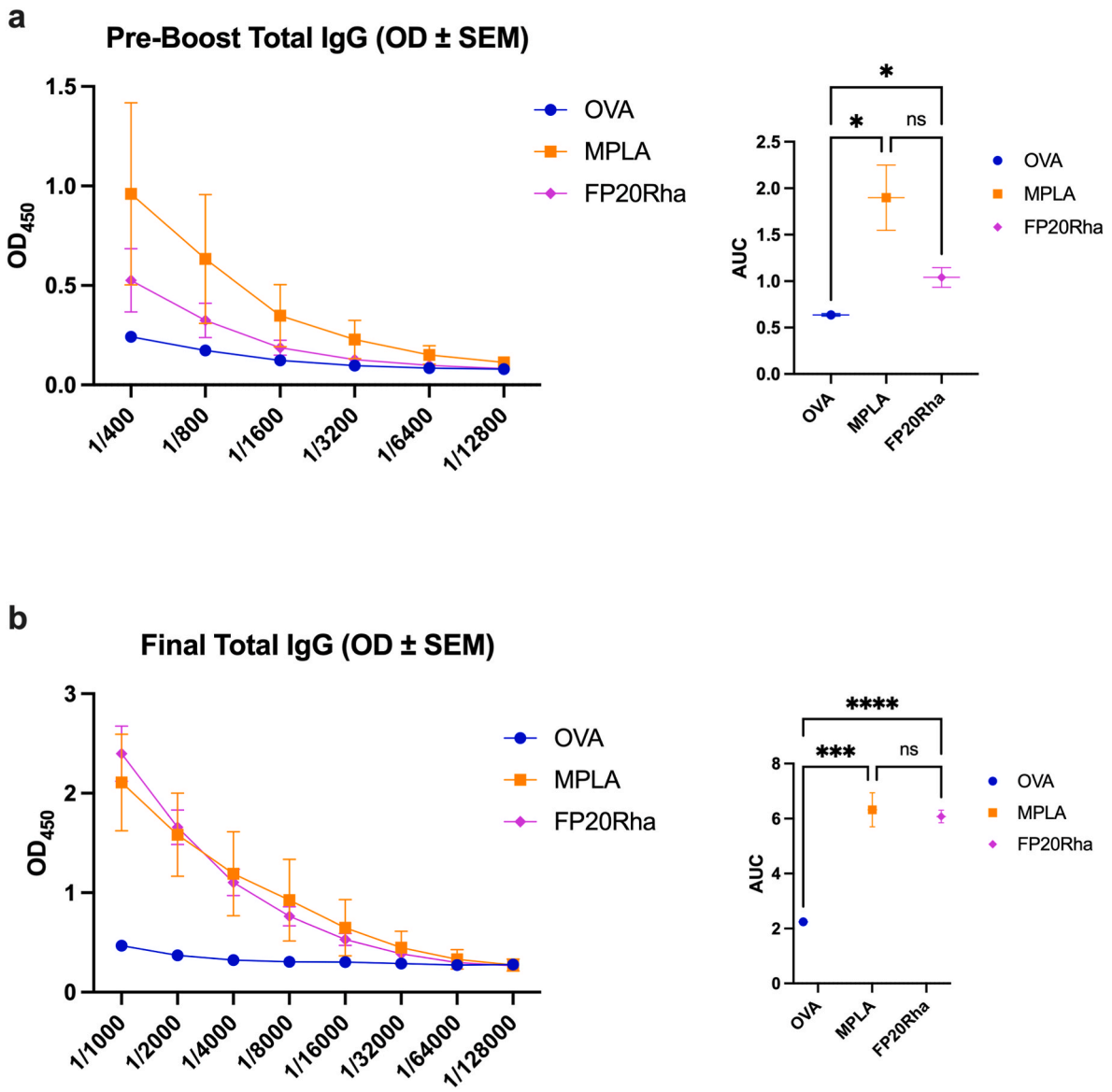

Fig. 3. - FP20Rha adjuvant activity in OVA vaccination experiments. C57BL/6 mice were immunized subcutaneously on days 1 and 21 with OVA formulated with or without MPLA, and FP20Rha as adjuvants. **a**) Total antibody response to prime OVA immunization 21 days post-prime immunization. **b**) Total antibody response to boost immunization 42 days post immunization. Values represent mean ± SEM. Brown–Forsythe and Welch one-way ANOVA tests (with an alpha of 0.05) were utilized to compare the areas under each curve. *p < 0.05; **p < 0.01; ***p < 0.001. n = 8 per group.

3.3. FTIR microspectroscopy characterization coupled to multivariate analysis of TDM cells treated with LPS, FP20Rha and FP20

After the validation of the model system by biological assays, TDM intact cells treated with LPS, FP20Rha and FP20 were subjected to FTIR microspectroscopy analysis. For simplicity sake, the mean second derivative of the absorption spectra (Figure S1) of cells treated with FP20Rha are shown in figures, compared with untreated (0h) ones. The spectral components that display a significant spectral variation evaluated by *t*-test analysis for each time-point compared to the untreated cells at the same time will be discussed. Moreover, the significance of the temporal evolution of the observed spectral changes was evaluated by the MANOVA analysis (Table S1).

In Fig. 4a, the second derivative analysis of the FTIR spectra of cells untreated (NT) and treated with FP20Rha is displayed in the spectral range between 3050 and 2800 cm^{-1}, where cell lipids mainly absorb. Particularly, the spectrum of NT cells (0h) is characterised by the methylene (at ~2922 and 2851 cm^{-1}) and methyl (at ~2958 and 2872 cm^{-1}) stretching vibrations of lipid hydrocarbon chains [28,29] (see Table S2 for a detailed assignment). A decrease in intensity of the CH_2 bands was detected at 15 min of treatment, followed by an increase at 3h, up to 24h, as shown in the box plot of Fig. S2, where the ratio between CH_2 and CH_3 intensities is reported. This spectral behavior is evident for LPS, as previously reported [6], and for FP20Rha, while it was less evident in the case of treatment with FP20 (Fig. S2). To get further information on possible lipid modifications induced by the treatment with the different molecules, we extended the IR analysis to the 1500-1200 cm^{-1} range (Fig. 4b), where significant changes were found at ~1467 cm^{-1}, mainly due to the overlapping CH_2 bending and CH_3 deformation vibrations [28,29]. The temporal behavior of its intensity variation resembles that observed for the CH_2/CH_3 ratio detected between 3050 and 2800 cm^{-1} (Fig. S2). Overall, the observed differences in the above spectral ranges, that point to modifications of the physico-chemical properties of cell lipids, impacting also membrane fluidity [6], indicate that the three molecules affect at a different extent the cell lipids (Fig. 4 and Fig. S2). Indeed, although not extensively

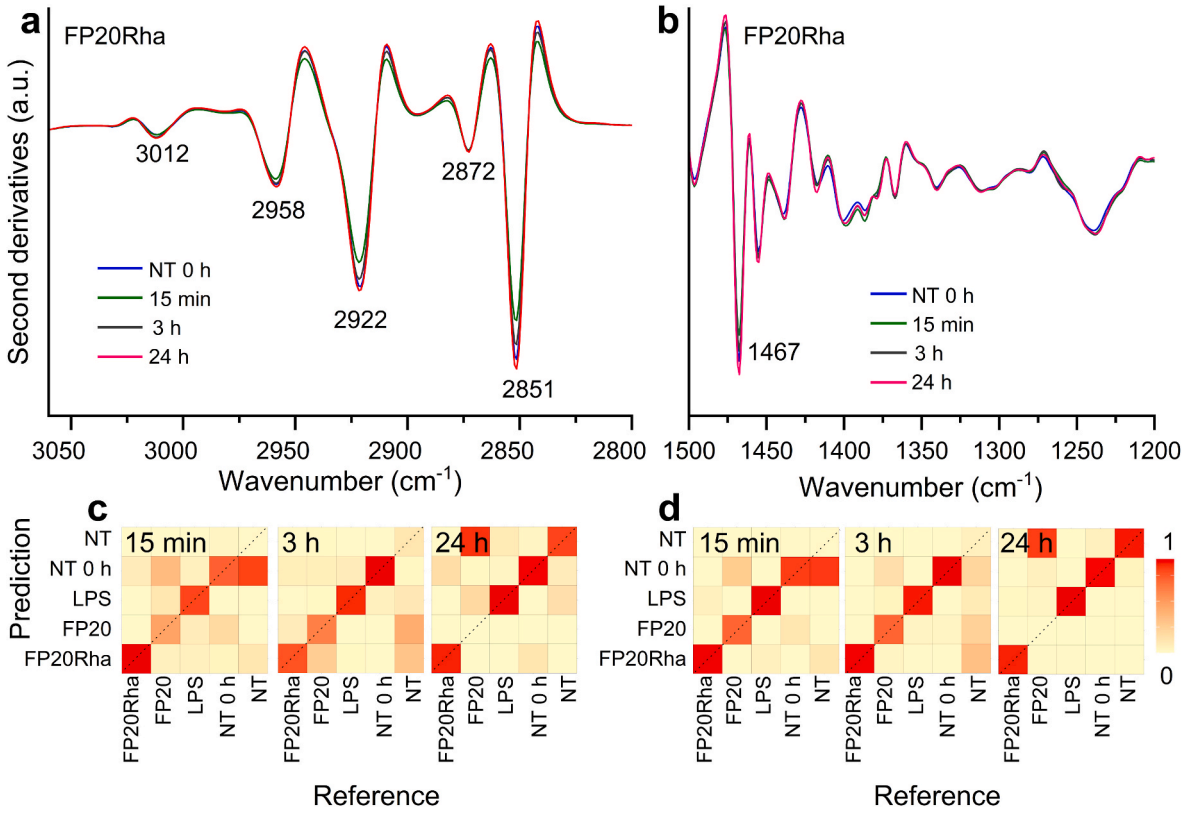

Fig. 4. FTIR analysis in the lipid absorption ranges of TDM cells treated with different TLR4 agonists. a,b) Mean second derivative spectra between 3050 and 2800 cm^{-1} (a) and 1500-1200 cm^{-1} (b) of TDM cells before and at different time points of treatment with FP20Rha. In the figures, the most relevant peak positions are indicated. **c, d)** Confusion matrices of the nnet analysis of TDM cells, untreated and at different time points of treatment with the different molecules, in the spectral ranges 3050-2800 cm^{-1} (c) and 1500-1200 cm^{-1} (d).

studied, lipids have been described as key players in LPS-induced response. It is known that TLR4 activation leads to synthesis of eicosanoids, sphingolipids and sterols and to an overall remodelling of the lipid profile in macrophages. Thus, the results reported here are possibly due to changes in lipid constituents involved in regulating pathogen-associated molecular pattern recognition, in this case LPS and FP compounds, and early proinflammatory response [30]. Furthermore, a particular subclass of lipids, phospholipids, are involved in regulating the synthesis of proinflammatory cytokines [31,32]. These FTIR data concerning lipids indicate clearly that the most active molecule FP20Rha behaves similarly to LPS while the less active FP20 affects macrophages more weakly, thus paralleling what it has been found in *in vitro* cytokine induction analysis in TDM cells.

Moreover, in particular for LPS, the spectral changes at ~3012 cm^{-1}, due to the stretching vibrations of the olefinic group (=CH) [28], - providing information on lipid hydrocarbon chain unsaturation degree - resulted to be significant (Fig. S2). This finding can be also related to lipid peroxidation and oxidative stress. Indeed, stimulation of macrophages with LPS has been linked to both events, due to the release of nitric oxide and reactive oxygen species [33,34]. This oxidative state is achieved after classic activation of macrophages and polarization towards a M1 phenotype, which leads to metabolic reprogramming of the cell with enhancement of glycolysis and fatty acid synthesis [30,32,35,36]. Furthermore, the production of proinflammatory cytokines, such as TNF, is linked to the formation of unsaturated lipid droplets [37]. These cellular changes triggered by LPS can be the driving force for changes in lipid content and unsaturation observed in FTIR analysis. Although to a lesser extent, as observed in Fig. S2, FP20Rha also induces such changes, suggesting that, as LPS, this new TLR4 agonist is able to induce M1 polarization, which is congruent with the presented cytokine profile.

To explore the possibility to discriminate among cells subjected to the treatment with the different molecules at different time points, we applied the neural network (nnet) multivariate analysis, whose confusion matrices and overall classification accuracies are reported in Fig. 4c,d and Fig. S3, respectively. The accuracy obtained in the two spectral ranges is satisfactory, being between 0.68 and 0.85 (Fig. S3). The confusion matrices indicate that a good classification of LPS and FP20Rha is obtained at all the analysed time points, while a relatively important misclassification was found for FP20 (see, for instance, 24h).

In Fig. 5a, we reported the second derivative analysis of the FTIR spectra of cells untreated (NT) and treated with FP20Rha between 1760 and 1600 cm^{-1}, mainly due to the C=O stretching vibrations of esters and of the peptide bond (Amide I band) [29,38]. Moreover, we also displayed the tyrosine band at ~1515 cm^{-1}. The second derivative spectrum of untreated cells (0h) is characterized by a band at ~ 1742 cm^{-1}, assigned mainly to ester carbonyl groups of lipids [28] (Table S2), whose intensity decreased at 15 min of treatment and then increased again up to the end of our observation (24h). The Amide I band, providing information on the whole cell protein secondary structures, is dominated by two peaks, at ~1655 cm^{-1}, mainly due to α-helices and random coils, and ~1639 cm^{-1}, assigned to β-sheet structures [29,38]. The Amide I spectral features are very similar at the different time points, strongly suggesting that the treatment with FP20Rha does not significantly affect the overall protein secondary structure content. As shown by the ratio between the 1655 cm^{-1} and the 1639 cm^{-1} intensities, also in the case of FP20 we did not observe any significant spectral changes, in contrast to what we have seen for LPS [6] (see box plots of Fig. S2 and Table S1a for the MANOVA analysis). Overall, a similar trend is visible in the increase of the 1655 cm^{-1}/1639 cm^{-1} ratio (Fig. S2), more evident in FP20Rha compared with FP20, suggesting that the former could induce increased overall changes in protein structure, but lower intensity than LPS (Fig. S2, Table S1a). This observation

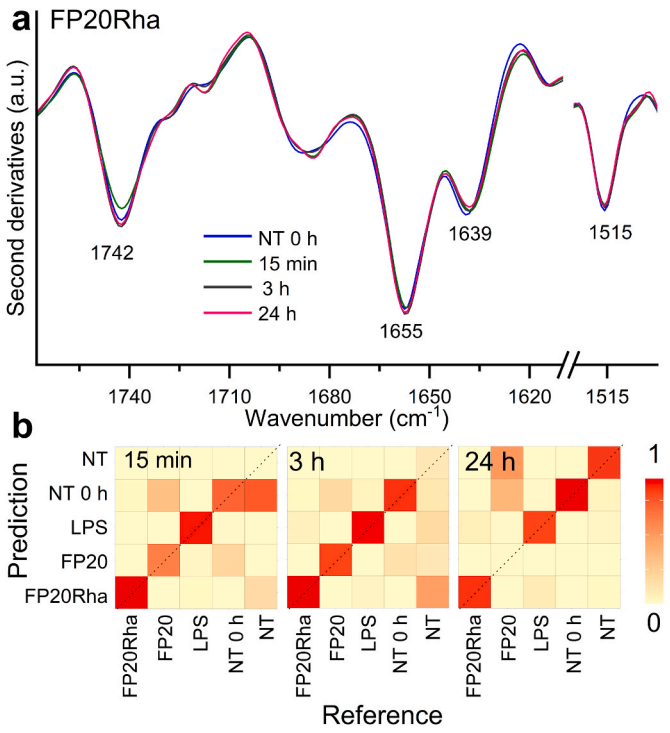

Fig. 5. FTIR analysis in the carbonyl absorption range of TDM cells treated with different TLR4 agonists. a) Mean second derivative spectra between 1760 and 1500 cm^{-1} of TDM cells before and at different time points of treatment with FP20Rha. In the figures, the most relevant peak positions are indicated. **b)** Confusion matrices of the nnet analysis of TDM cells, untreated and at different time points of treatment with the different molecules.

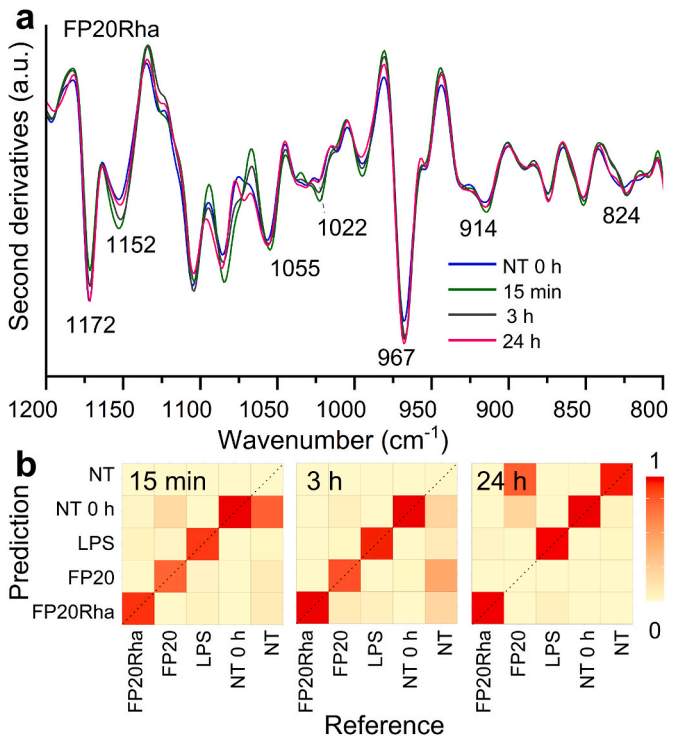

Fig. 6. FTIR analysis in the fingerprint region of TDM cells treated with different TLR4 agonists. a) Mean second derivative spectra between 1200 and 800 cm^{-1} of TDM cells before and at different time points of treatment with FP20Rha. In the figures, the most relevant peak positions are indicated. **b)** Confusion matrices of the nnet analysis of TDM cells, untreated and at different time points of treatment with the different molecules.

suggests that FP20Rha is able to induce a more potent response than FP20 in treated cells, thus reflecting *in vitro* and *in vivo* data.

Interestingly, the temporal behavior of the ratio between the lipid ester (1742 cm^{-1}) and the tyrosine (1515 cm^{-1}) band intensities resembles that observed for the lipid analysis (Fig. 4 and Fig. S2). Taken together, these results indicate that the cell response induced by the treatment in particular with LPS and FP20Rha involves mainly lipid components.

Nnet analysis in this spectral region shows a satisfactory discrimination accuracy (between 0.77 and 0.82), with a better classification in the case of LPS and FP20Rha (Fig. S3).

Fig. 6a displays the second derivative analysis of the FTIR spectra of cells untreated (NT) and treated with FP20Rha in the fingerprint region, dominated by the absorption of complex carbohydrate modes that overlap vibrations also from nucleic acids, lipids and phosphates (Table S2). The untreated cell derivative spectrum (0h) shows a component at ~ 1172 cm^{-1} which can be assigned to different biomolecule moieties [28,29,39–44] (Table S2). Since its intensity variation induced by the treatment with the three molecules is synchronous with that of the other bands mainly ascribable to lipids (Fig. 4 and Fig. S2), this peak can be tentatively mainly assigned to lipid moieties [28,29,39] (box plots in Fig. S2, Table S2 [6] and references therein). Moreover, this absorption falls in a spectral region associated with different vibrational modes from carbohydrates and glycosaminoglycans (GAGs), both sulfated and non-sulfated [40–42] (Table S2). Furthermore, the ~1172 cm^{-1} peak has also been associated to non-hydrogen bonded C–O of the C–OH groups of serine, threonine and tyrosine residues [43,44]. Then, the ~1152 cm^{-1} peak, which is mainly due to vibrations of carbohydrates, including GAGs, has been also assigned to hydrogen-bonded C–O groups of serine, threonine, and tyrosine [40–44]. Therefore, considering the simultaneous and opposite direction of the intensity changes of the 1172 cm^{-1} and 1152 cm^{-1} peaks, their relative variation could also provide evidence of phosphorylation events [43,44] induced by the different cell treatments (Table S2). As reported in the box plot of Fig. S2, these two bands are significant in particular for LPS and FP20Rha. Phosphorylations of serine, threonine and tyrosine are involved in cell signalling and lead to different cellular events such as degradation, aggregation and translocation [45,46]. Particularly in TLR4 agonism, such as the one induced by LPS, this post-translational modification is involved in the activation of different proteins throughout the downstream TLR4-dependent signalling and during the whole studied time points [47,48]. In addition, the ~1055 cm^{-1}, ~1022 cm^{-1} and the ~914 cm^{-1} components are mainly ascribable to vibrations of carbohydrates, including GAGs [40–42]. The 1055 and 1022 cm^{-1} peaks are associated also to glycosylated lipids and proteins [49,50] (Table S2).

Moreover, the intense 967 cm^{-1} band can be mainly associated with the stretching of the $N(CH_3)_3$ group, typical of phosphatidylcholine (PC) and sphingomyelin [28,29]. Then, we cannot exclude a contribution of DNA/RNA vibrations to this absorption [51] (Table S2).

Finally, as already discussed previously for the LPS treatment [6], a large absorption between ~838 and ~805 cm^{-1} is observed that becomes more resolved after treatment (peak at ~824 cm^{-1}), which could be assigned to differences in the configuration of polysaccharide glycosidic linkages and to sulfated GAG vibrations [40,52–54] (Table S2).

Overall, the FTIR and multivariate analysis findings in the fingerprint region highlight the resemblance between LPS and FP20Rha-induced responses and the difference between FP20Rha and FP20-induced responses. Indeed, both LPS and FP20Rha lead to changes in GAGs composition within the cell and, once again, lipid contribution is highlighted. GAGs are linear polysaccharides involved in different biological functions due to their interactions with different targets such as proteins, cytokines, chemokines and others [55]. Changes in structure

and sulfation of GAGs, mediated by sulfotransferases, occur during macrophage polarization towards a M1 proinflammatory phenotype [56]. Due to its similarity to LPS in FTIR analysis, we can speculate that FP20Rha is able to induce similar phosphorylations as LPS in the presented time points, indicating that this compound might trigger the same activations in TLR4-signaling.

Consistently with what found for the other analysed spectral ranges, the nnet analysis in the fingerprint region (Fig. S3) led to a high discrimination accuracy (0.82–0.85), with confusion matrices (Fig. 6b) indicating a clear classification of cells treated with FP20Rha and LPS on one hand, and a misclassification of FP20 particularly at 24h.

Considering the overall significant spectral changes induced by the different cell treatments, involving different biomolecule classes, in Fig. 7 we have calculated the relative spectral distances between untreated and treated cells, for each molecule and time point of treatment, by PLS-DA analysis. As shown, the treatment with LPS and FP20Rha led to higher distances compared to the untreated cells, at each time. FP20 resulted to be closer to control cells, particularly at 24h, in agreement with nnet confusion matrices.

Therefore, the nnet and PLS-DA analyses of the FTIR data show that FP20Rha and LPS have a higher level of activity on TDM cells compared to FP20, which is consistent with the presented *in vitro* and *in vivo* data.

A closer inspection of the significant spectral changes highlighted peculiar molecular cellular signatures triggered by the different treatments. In particular, the cell response to LPS and FP20Rha involved the vibrational fingerprint related to physico-chemical variations in lipids. These findings suggest that FP20Rha has a similar effect on cellular lipids as LPS, while FP20 differs from both molecules. Moreover, the perturbation of the Amide I band in the LPS treated cell spectrum indicates that this molecule also impacts the overall protein secondary structures, which might reflect the synthesis of new proteins. The observed trend (see box plot of Fig. S2 and Table S1a for the MANOVA analysis where the P-value of the interaction treatment-time is much lower than the 0.01 threshold) suggests that the impact on protein structure is higher in FP20Rha-treated TDM than in FP20-treated ones.

The investigation of the complex fingerprint region, providing mainly information on glycan modifications (GAGs, glycoproteins, glycolipids, etc.) and protein phosphorylation (Table S2), sheds light on a peculiar spectroscopic pattern for each treatment that points to significant differences in the biochemical profile induced by the investigated molecules. Significant changes in these biomolecules can be related to the inflammation process, since they are essential for inflammatory signalling.

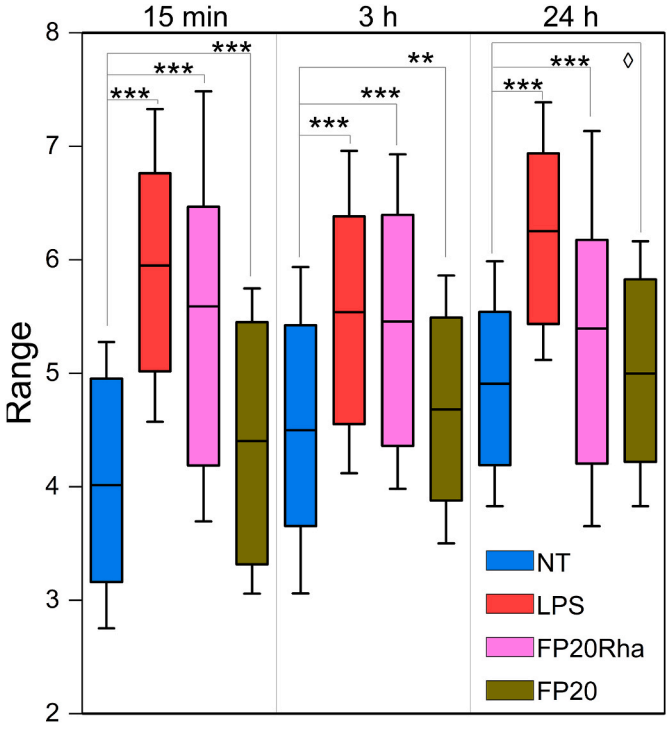

Fig. 7. Box plots representing the distribution of distances among spectra in the low dimensional PLS-DA score space. Distances have been computed between the untreated cells and the treated cells at each time point. ◇p > 0.05; **p < 0.01; ***p < 0.001.

4. Conclusions

FTIR spectroscopy is currently emerging as a valuable tool to obtain a comprehensive molecular fingerprint of intact cells, without requiring sample labeling and/or pre-processing steps that could induce artefacts. This vibrational tool provides, within a single measurement, information on the content and structure of the main biomolecules, a feature that is hardly obtainable with other techniques. In the present manuscript, we compared the human TDM cell response to LPS with those of two rationally designed TLR4 agonists, FP20 and FP20Rha, using cell biology techniques and by their molecular spectroscopic fingerprint. Noteworthy, the spectroscopic fingerprint of the treated cells allowed the identification of IR bands (and, therefore, of the main biomolecules responsible for), which showed similar or dissimilar variations among the different treatments. In particular, lipids and glycans were found to be involved in the LPS and FP20Rha response to a comparable extent. In this proof-of-concept study, the application of machine learning approaches made it possible to evaluate in an unbiased way the distances in the molecular signatures of the cells treated with the different molecules, disclosing the similarity between LPS and FP20Rha and the differences between FP20Rha and its parent compound FP20. This is in very good agreement with the higher activity of FP20Rha over FP20 in stimulating TLR4-dependent cytokine production in TDM and in the immune response to OVA antigen *in vivo*.

The use of FTIR analysis for the *in situ* screening of bioactive compounds and pharmacological hit selection is still pioneristic [57]. Compared to other biochemical and cellular methods used for compound screening and preclinical hit selection, FTIR analysis presents several peculiar advantages and strengths. Its high sensitivity allows detection of changes in cellular molecular signatures in response to the treatment with drug candidates on intact cells, without requiring labeling or extraction procedures. The possibility to have a wide snapshot of the cellular processes affected and triggered by the molecule provides untargeted preliminary information on a drug's (or drug hit) mechanism of action.

In the drug discovery process, the identification of a hit candidate and the study of its mechanism of action are normally two distinct phases, the first being based on a high-throughput test and the latter requiring more extensive and time-consuming biochemical and cellular characterization. We propose here the use of FTIR spectroscopy supported by AI and multivariate analysis approaches [14,58] to achieve a more holistic understanding of the cell response to new drug candidates while screening them in cells, gathering preliminary mechanistic insights in an easier, faster and less expensive way than traditional methods.

While the proposed approach is straightforward, label free, untargeted, and does not require extensive sample preparation, the throughput is, however, limited. Potentially, our proof-of-concept study can be further developed by incorporating recent high-throughput technologies for IR spectra collection and analysis [59–61]. This could mean in the very near future, an emerging technique in the field of screening of new proinflammatory drug candidates.

CRediT authorship contribution statement

Diletta Ami: Writing – review & editing, Writing – original draft,

Visualization, Methodology, Investigation, Formal analysis, Data curation, Conceptualization. **Ana Rita Franco:** Writing – review & editing, Writing – original draft, Visualization, Methodology, Investigation, Formal analysis, Data curation. **Valentina Artusa:** Writing – review & editing, Methodology, Investigation. **Alessio Romerio:** Investigation. **Mohammed Monsoor Shaik:** Investigation. **Alice Italia:** Investigation. **Juan Anguita:** Visualization, Methodology, Investigation. **Samuel Pasco:** Visualization, Methodology, Investigation. **Paolo Mereghetti:** Writing – review & editing, Writing – original draft, Methodology, Formal analysis. **Francesco Peri:** Writing – review & editing, Writing – original draft, Supervision, Resources, Project administration, Funding acquisition, Conceptualization. **Antonino Natalello:** Writing – review & editing, Writing – original draft, Visualization, Validation, Supervision, Resources, Project administration, Methodology, Funding acquisition, Formal analysis, Data curation, Conceptualization.

Declaration of competing interest

The authors declare the following financial interests/personal relationships which may be considered as potential competing interests. Antonino Natalello reports financial support was provided by University of Milano-Bicocca, Department of Biotechnology and Biosciences. Francesco Peri reports financial support was provided by University of Milano-Bicocca, Department of Biotechnology and Biosciences. Francesco Peri has patent #New synthetic agonists of TLR4 receptor licensed to Licensee. If there are other authors, they declare that they have no known competing financial interests or personal relationships that could have appeared to influence the work reported in this paper.

Data availability

Data will be made available on request.

Acknowledgements

This work was supported by the MSCA-ETN project BactiVax GA No. 860325 (H2020, EU), the Italian consortium CINMPIS, and the University of Milano-Bicocca (Fondo di Ateneo per la Ricerca). The graphical abstract was created with BioRender.com (Agreement number: UA26NLS3F0).

Appendix A. Supplementary data

Supplementary data to this article can be found online at https://doi.org/10.1016/j.talanta.2024.126104.

References

[1] B. Pulendran, S.P. Arunachalam, D.T. O'Hagan, Emerging concepts in the science of vaccine adjuvants, Nat. Rev. Drug Discov. 20 (2021) 454–475, https://doi.org/10.1038/s41573-021-00163-y.

[2] A. Romerio, F. Peri, Increasing the chemical variety of small-molecule-based TLR4 modulators: an overview, Front. Immunol. 11 (2020) 1210, https://doi.org/10.3389/fimmu.2020.01210.

[3] A. Farias, A. Soto, F. Puttur, C.J. Goldin, S. Sosa, C. Gil, F.A. Goldbaum, P. M. Berguer, A TLR4 agonist improves immune checkpoint blockade treatment by increasing the ratio of effector to regulatory cells within the tumor microenvironment, Sci. Rep. 11 (2021) 15406, https://doi.org/10.1038/s41598-021-94837-7.

[4] J.-K. Ryu, S.J. Kim, S.-H. Rah, J.I. Kang, H.E. Jung, D. Lee, H.K. Lee, J.-O. Lee, B. S. Park, T.-Y. Yoon, H.M. Kim, Reconstruction of LPS transfer cascade reveals structural determinants within LBP, CD14, and TLR4-MD2 for efficient LPS recognition and transfer, Immunity 46 (2017) 38–50, https://doi.org/10.1016/j.immuni.2016.11.007.

[5] P.J. Murray, Macrophage polarization, Annu. Rev. Physiol. 79 (2017) 541–566, https://doi.org/10.1146/annurev-physiol-022516-034339.

[6] D. Ami, A.R. Franco, V. Artusa, P. Mereghetti, F. Peri, A. Natalello, A global picture of molecular changes associated to LPS treatment in THP-1 derived human macrophages by fourier transform infrared microspectroscopy, Int. J. Mol. Sci. 23 (2022), https://doi.org/10.3390/ijms232113447.

[7] B. Dunkhunthod, C. Talabnin, M. Murphy, K. Thumanu, P. Sittisart, G. Eumkeb, (Lour.) decne. Extract alleviates oxidative stress and inflammatory mediators produced by RAW264.7 macrophages, Oxid. Med. Cell. Longev. 2021 (2021) 8658314, https://doi.org/10.1155/2021/8658314.

[8] A. Paemanee, S. Rattanabunyong, Y. Ketngamkum, J. Siriwaseree, P. Pongpamorn, K. Romyanon, S. Tangphatsornruang, B. Kuaprasert, K. Choowongkomon, Mass spectrometry and synchrotron-FTIR microspectroscopy reveal the anti-inflammatory activity of Bua Bok extracts, Phytochem. Anal. 33 (2022) 1086–1098, https://doi.org/10.1002/pca.3161.

[9] I.W. Levin, R. Bhargava, Fourier transform infrared vibrational spectroscopic imaging: integrating microscopy and molecular recognition, Annu. Rev. Phys. Chem. 56 (2005) 429–474, https://doi.org/10.1146/annurev.physchem.56.092503.141205.

[10] S.G. Kazarian, K.L.A. Chan, Applications of ATR-FTIR spectroscopic imaging to biomedical samples, Biochim. Biophys. Acta 1758 (2006) 858–867, https://doi.org/10.1016/j.bbamem.2006.02.011.

[11] D. Ami, P. Mereghetti, A. Natalello, Contribution of infrared spectroscopy to the understanding of amyloid protein aggregation in complex systems, Front. Mol. Biosci. 9 (2022) 822852, https://doi.org/10.3389/fmolb.2022.822852.

[12] L. Wang, B. Mizaikoff, Application of multivariate data-analysis techniques to biomedical diagnostics based on mid-infrared spectroscopy, Anal. Bioanal. Chem. 391 (2008) 1641–1654, https://doi.org/10.1007/s00216-008-1989-9.

[13] M.J. Baker, J. Trevisan, P. Bassan, R. Bhargava, H.J. Butler, K.M. Dorling, P. R. Fielden, S.W. Fogarty, N.J. Fullwood, K.A. Heys, C. Hughes, P. Lasch, P. L. Martin-Hirsch, B. Obinaju, G.D. Sockalingum, J. Sulé-Suso, R.J. Strong, M. J. Walsh, B.R. Wood, P. Gardner, F.L. Martin, Using Fourier transform IR spectroscopy to analyze biological materials, Nat. Protoc. 9 (2014) 1771–1791, https://doi.org/10.1038/nprot.2014.110.

[14] C.L.M. Morais, K.M.G. Lima, M. Singh, F.L. Martin, Tutorial: multivariate classification for vibrational spectroscopy in biological samples, Nat. Protoc. 15 (2020) 2143–2162, https://doi.org/10.1038/s41596-020-0322-8.

[15] D. Ami, P. Mereghetti, S.M. Doglia, Multivariate analysis for Fourier transform infrared spectra of complex biological systems and processes, in: Multivariate Analysis in Management, Engineering and the Sciences, InTech, 2013, https://doi.org/10.5772/53850.

[16] F.A. Facchini, A. Minotti, A. Luraghi, A. Romerio, N. Gotri, A. Matamoros-Recio, A. Iannucci, C. Palmer, G. Wang, R. Ingram, S. Martin-Santamaria, G. Pirianov, M. De Andrea, M.A. Valvano, F. Peri, Synthetic glycolipids as molecular vaccine adjuvants: mechanism of action in human cells and in vivo activity, J. Med. Chem. 64 (2021) 12261–12272, https://doi.org/10.1021/acs.jmedchem.1c00896.

[17] A. Romerio, N. Gotri, A.R. Franco, V. Artusa, M.M. Shaik, S.T. Pasco, U. Atxabal, A. Matamoros-Recio, M. Mínguez-Toral, J.D. Zalamea, A. Franconetti, N.G. A. Abrescia, J. Jimenez-Barbero, J. Anguita, S. Martín-Santamaría, F. Peri, New glucosamine-based TLR4 agonists: design, synthesis, mechanism of action, and in vivo activity as vaccine adjuvants, J. Med. Chem. 66 (2023) 3010–3029, https://doi.org/10.1021/acs.jmedchem.2c01998.

[18] A. Romerio, A.R. Franco, M. Shadrick, M.M. Shaik, V. Artusa, A. Italia, F. Lami, A. V. Demchenko, F. Peri, Overcoming challenges in chemical glycosylation to achieve innovative vaccine adjuvants possessing enhanced TLR4 activity, ACS Omega 8 (2023) 36412–36417, https://doi.org/10.1021/acsomega.3c05363.

[19] A.R. Franco, O. Sadones, A. Romerio, V. Artusa, M.M. Shaik, S.T. Pasco, A. Italia, S. D'Amato, J. Anguita, J. Huebner, F. Romero-Saavedra, F. Peri, Novel TLR4-activating vaccine adjuvant enhances the production of Enterococcus faecium-binding antibodies, J. Med. Chem. (2024), https://doi.org/10.1021/acs.jmedchem.3c02215.

[20] D. Ami, A. Natalello, S.M. Doglia, Fourier transform infrared microspectroscopy of complex biological systems: from intact cells to whole organisms, Methods Mol. Biol. 895 (2012) 85–100, https://doi.org/10.1007/978-1-61779-927-3_7.

[21] R Core Team, R, A Language and Environment for Statistical Computing, R Foundation for Statistical Computing, Vienna, Austria, 2021. https://www.R-project.org/. (Accessed 17 November 2023).

[22] M. Kuhn, Building predictive models in R using the caret package, J. Stat. Software 28 (2008) 1–26, https://doi.org/10.18637/jss.v028.i05.

[23] L. Breiman, J.H. Friedman, R.A. Olshen, C.J. Stone, Classification and Regression Trees, Chapman & Hall/CRC, 2017, https://doi.org/10.1201/9781315139470.

[24] G.D. Garson, Interpreting neural-network connection weights, AI Expert 6 (1991) 46–51. https://dl.acm.org/doi/abs/10.5555/129449.129452.

[25] A.T.C. Goh, Back-propagation neural networks for modeling complex systems, Artif. Intell. Eng. 9 (1995) 143–151, https://doi.org/10.1016/0954-1810(94)00011-S.

[26] M. Pérez-Enciso, M. Tenenhaus, Prediction of clinical outcome with microarray data: a partial least squares discriminant analysis (PLS-DA) approach, Hum. Genet. 112 (2003) 581–592, https://doi.org/10.1007/s00439-003-0921-9.

[27] B.G. Tabachnick, L.S. Fidell, Using Multivariate Statistics, Pearson Education, 2013. https://play.google.com/store/books/details?id=ucj1ygAACAAJ.

[28] H.L. Casal, H.H. Mantsch, Polymorphic phase behaviour of phospholipid membranes studied by infrared spectroscopy, Biochim. Biophys. Acta 779 (1984) 381–401, https://doi.org/10.1016/0304-4157(84)90017-0.

[29] L.K. Tamm, S.A. Tatulian, Infrared spectroscopy of proteins and peptides in lipid bilayers, Q. Rev. Biophys. 30 (1997) 365–429, https://doi.org/10.1017/s0033583597003375.

[30] A. Batista-Gonzalez, R. Vidal, A. Criollo, L.J. Carreño, New insights on the role of lipid metabolism in the metabolic reprogramming of macrophages, Front. Immunol. 10 (2019) 2993, https://doi.org/10.3389/fimmu.2019.02993.

[31] J.W. Lee, H.J. Mok, D.Y. Lee, S.C. Park, G.-S. Kim, S.-E. Lee, Y.-S. Lee, K.P. Kim, H. D. Kim, UPLC-QqQ/MS-based lipidomics approach to characterize lipid alterations

in inflammatory macrophages, J. Proteome Res. 16 (2017) 1460–1469, https://doi.org/10.1021/acs.jproteome.6b00848.
[32] A. Marrocco, L.A. Ortiz, Role of metabolic reprogramming in pro-inflammatory cytokine secretion from LPS or silica-activated macrophages, Front. Immunol. 13 (2022) 936167, https://doi.org/10.3389/fimmu.2022.936167.
[33] O.A. Castaneda, S.-C. Lee, C.-T. Ho, T.-C. Huang, Macrophages in oxidative stress and models to evaluate the antioxidant function of dietary natural compounds, J. Food Drug Anal. 25 (2017) 111–118, https://doi.org/10.1016/j.jfda.2016.11.006.
[34] Z. Gou, S. Jiang, C. Zheng, Z. Tian, X. Lin, Equol inhibits LPS-induced oxidative stress and enhances the immune response in chicken HD11 macrophages, Cell. Physiol. Biochem. 36 (2015) 611–621, https://doi.org/10.1159/000430124.
[35] A. Shapouri-Moghaddam, S. Mohammadian, H. Vazini, M. Taghadosi, S.-A. Esmaeili, F. Mardani, B. Seifi, A. Mohammadi, J.T. Afshari, A. Sahebkar, Macrophage plasticity, polarization, and function in health and disease, J. Cell. Physiol. 233 (2018) 6425–6440, https://doi.org/10.1002/jcp.26429.
[36] A. Remmerie, C.L. Scott, Macrophages and lipid metabolism, Cell. Immunol. 330 (2018) 27–42, https://doi.org/10.1016/j.cellimm.2018.01.020.
[37] K. Czamara, M. Stojak, M.Z. Pacia, A. Zieba, M. Baranska, S. Chlopicki, A. Kaczor, Lipid droplets formation represents an integral component of endothelial inflammation induced by LPS, Cells 10 (2021), https://doi.org/10.3390/cells10061403.
[38] A. Barth, Infrared spectroscopy of proteins, Biochim. Biophys. Acta 1767 (2007) 1073–1101, https://doi.org/10.1016/j.bbabio.2007.06.004.
[39] E. Gazi, J. Dwyer, N.P. Lockyer, P. Gardner, J.H. Shanks, J. Roulson, C.A. Hart, N. W. Clarke, M.D. Brown, Biomolecular profiling of metastatic prostate cancer cells in bone marrow tissue using FTIR microspectroscopy: a pilot study, Anal. Bioanal. Chem. 387 (2007) 1621–1631, https://doi.org/10.1007/s00216-006-1093-y.
[40] M. Kacuráková, P. Capek, V. Sasinková, N. Wellner, A. Ebringerová, FT-IR study of plant cell wall model compounds: pectic polysaccharides and hemicelluloses, Carbohydr. Polym. 43 (2000) 195–203, https://doi.org/10.1016/s0144-8617(00)00151-x.
[41] S. Brézillon, V. Untereiner, L. Lovergne, I. Tadeo, R. Noguera, F.-X. Maquart, Y. Wegrowski, G.D. Sockalingum, Glycosaminoglycan profiling in different cell types using infrared spectroscopy and imaging, Anal. Bioanal. Chem. 406 (2014) 5795–5803, https://doi.org/10.1007/s00216-014-7994-2.
[42] H.T. Mohamed, V. Untereiner, G. Cinque, S.A. Ibrahim, M. Götte, N.Q. Nguyen, R. Rivet, G.D. Sockalingum, S. Brézillon, Infrared microspectroscopy and imaging analysis of inflammatory and non-inflammatory breast cancer cells and their GAG secretome, Molecules 25 (2020), https://doi.org/10.3390/molecules25184300.
[43] P.T. Wong, R.K. Wong, T.A. Caputo, T.A. Godwin, B. Rigas, Infrared spectroscopy of exfoliated human cervical cells: evidence of extensive structural changes during carcinogenesis, Proc. Natl. Acad. Sci. U.S.A. 88 (1991) 10988–10992, https://doi.org/10.1073/pnas.88.24.10988.
[44] D. Ami, P. Mereghetti, M. Leri, S. Giorgetti, A. Natalello, S.M. Doglia, M. Stefani, M. Bucciantini, A FTIR microspectroscopy study of the structural and biochemical perturbations induced by natively folded and aggregated transthyretin in HL-1 cardiomyocytes, Sci. Rep. 8 (2018) 12508, https://doi.org/10.1038/s41598-018-30995-5.
[45] T. Pawson, J.D. Scott, Protein phosphorylation in signaling–50 years and counting, Trends Biochem. Sci. 30 (2005) 286–290, https://doi.org/10.1016/j.tibs.2005.04.013.
[46] F. Ardito, M. Giuliani, D. Perrone, G. Troiano, L. Lo Muzio, The crucial role of protein phosphorylation in cell signaling and its use as targeted therapy, Int. J. Mol. Med. 40 (2017) 271–280, https://doi.org/10.3892/ijmm.2017.3036 (Review).
[47] W. Piao, C. Song, H. Chen, L.M. Wahl, K.A. Fitzgerald, L.A. O'Neill, A.E. Medvedev, Tyrosine phosphorylation of MyD88 adapter-like (mal) is critical for signal transduction and blocked in endotoxin tolerance, J. Biol. Chem. 283 (2008) 3109–3119, https://doi.org/10.1074/jbc.m707400200.
[48] Y. Li, H. Zhang, A.K. Kosturakis, R.M. Cassidy, H. Zhang, R.M. Kennamer-Chapman, A.B. Jawad, C.M. Colomand, D.S. Harrison, P.M. Dougherty, MAPK signaling downstream to TLR4 contributes to paclitaxel-induced peripheral neuropathy, Brain Behav. Immun. 49 (2015) 255–266, https://doi.org/10.1016/j.bbi.2015.06.003.
[49] C. Kirschbaum, K. Greis, E. Mucha, L. Kain, S. Deng, A. Zappe, S. Gewinner, W. Schöllkopf, G. von Helden, G. Meijer, P.B. Savage, M. Marianski, L. Teyton, K. Pagel, Unravelling the structural complexity of glycolipids with cryogenic infrared spectroscopy, Nat. Commun. 12 (2021) 1201, https://doi.org/10.1038/s41467-021-21480-1.
[50] A. Derenne, K.-M. Derfoufi, B. Cowper, C. Delporte, E. Goormaghtigh, FTIR spectroscopy as an analytical tool to compare glycosylation in therapeutic monoclonal antibodies, Anal. Chim. Acta 1112 (2020) 62–71, https://doi.org/10.1016/j.aca.2020.03.038.
[51] M. Banyay, M. Sarkar, A. Gräslund, A library of IR bands of nucleic acids in solution, Biophys. Chem. 104 (2003) 477–488, https://doi.org/10.1016/s0301-4622(03)00035-8.
[52] A. Synytsya, J. Čopíková, P. Matějka, V. Machovič, Fourier transform Raman and infrared spectroscopy of pectins, Carbohydr. Polym. 54 (2003) 97–106, https://doi.org/10.1016/s0144-8617(03)00158-9.
[53] F. Parker, Applications of Infrared Spectroscopy in Biochemistry, Biology, and Medicine, Springer, New York, NY, 2012, https://doi.org/10.1007/978-1-4684-1872-9.
[54] F. Cabassi, B. Casu, A.S. Perlin, Infrared absorption and Raman scattering of sulfate groups of heparin and related glycosaminoglycans in aqueous solution, Carbohydr. Res. 63 (1978) 1–11, https://doi.org/10.1016/S0008-6215(00)80924-6.
[55] S. Morla, Glycosaminoglycans and glycosaminoglycan mimetics in cancer and inflammation, Int. J. Mol. Sci. 20 (2019), https://doi.org/10.3390/ijms20081963.
[56] Z. Li, K.M. Bratlie, The influence of polysaccharides-based material on macrophage phenotypes, Macromol. Biosci. 21 (2021) e2100031, https://doi.org/10.1002/mabi.202100031.
[57] P.N. Sousa Sampaio, C.R.C. Calado, Antimicrobial evaluation of the Cynara cardunculus extract in Helicobacter pylori cells using mid-infrared spectroscopy and chemometric methods, J. Appl. Microbiol. 133 (2022) 1743–1756, https://doi.org/10.1111/jam.15679.
[58] R. Cardoso Rial, AI in analytical chemistry: advancements, challenges, and future directions, Talanta 274 (2024) 125949, https://doi.org/10.1016/j.talanta.2024.125949.
[59] H.J. Butler, P.M. Brennan, J.M. Cameron, D. Finlayson, M.G. Hegarty, M. D. Jenkinson, D.S. Palmer, B.R. Smith, M.J. Baker, Development of high-throughput ATR-FTIR technology for rapid triage of brain cancer, Nat. Commun. 10 (2019) 4501, https://doi.org/10.1038/s41467-019-12527-5.
[60] F.L. Martin, Translating biospectroscopy techniques to clinical settings: a new paradigm in point-of-care screening and/or diagnostics, J. Personalized Med. 13 (2023), https://doi.org/10.3390/jpm13101511.
[61] B. Ribeiro da Cunha, L.P. Fonseca, C.R.C. Calado, Metabolic fingerprinting with fourier-transform infrared (FTIR) spectroscopy: towards a high-throughput screening assay for antibiotic discovery and mechanism-of-action elucidation, Metabolites 10 (2020), https://doi.org/10.3390/metabo10040145.